

The influence of electric loading on crack paths in ferroelectrics

Zhibin Wang^{a,*}, Andreas Ricoeur^a

^aUniversity of Kassel, Institute of Mechanics, Mönchebergstraße 7, 34125 Kassel, Germany

Abstract

Ferroelectric materials are widely used in our daily life and many advanced industrial products. The understanding of their fracture behavior has been in the focus of research for decades, since the success of their application requires reliability and durability. For ferroelectric fracture behavior, different fracture criteria have been proposed and the influence of various mechanical-electric loading combinations on crack propagation have been investigated. However, the crack path and the deflection of crack propagation in ferroelectrics are still not satisfactorily understood. In this work, a three-point bending test for specimens of polarized PZT-5H with off-center notches is set up. Besides a pure mechanical loading, positive and negative electric fields below the coercive field are applied. Since the initial crack is not aligned with the mechanical loading axis, the crack does not propagate straightforwardly. A variety of crack paths are compared and statistically evaluated, illuminating the influence of electric loading. Recordings with a high-speed camera reveal unexpected details of crack initiation and growth. A modified J -integral vector criterion considering just the mechanical part of the driving force is proposed for numerical analyses of crack paths in piezoelectrics. The results of simulations based on this and other deflection criteria are finally compared to the experimental findings.

Keywords: piezoelectric material, crack propagation and arrest, crack deflection, mechanical testing

1. Introduction

Having been discovered in the early 1920s and intensively studied during the past several decades [1, 2], ferroelectric materials are nowadays found in many applications, e.g., sensors, actuators,

*Corresponding author
Email address: zhibin.wang@uni-kassel.de (Zhibin Wang)

RAM/memories, energy harvesters or transducers. Meanwhile, the mechanical reliability and durability of ferroelectric devices is of great concern. Depending on their specific utilization, the ferroelectric devices are exposed to mechanical loading, combined with e.g. cyclic electric loading or various other loading conditions, making the assessment of lifetime and structural reliability more complex due to different mechanisms of mechanical-electric coupling. The fracture behavior of ferroelectrics thus cannot be investigated within the framework of the fracture theory for conventional non-functional materials. It must rather be generalized, taking into account many factors, e.g., electric field induced elastic and inelastic strain, the permeability of the crack or the local state of polarization.

For the sake of a better fracture mechanical understanding, much experimental and analytical work has been done. The fracture toughness of two essential ferroelectrics, lead zirconate titanate (PZT) and the lead-free barium titanate (BT), the latter class of materials recently becoming more popular, has been measured by Vickers indentation tests in [3, 4, 5], which also revealed that the unpoled ferroelectrics are isotropic whereas the poled ferroelectrics behave anisotropically. The anisotropy of the fracture toughness, leading to a longer crack perpendicular to the poling direction and to a shorter one in parallel direction, is due to the switching-induced tensile or compressive stresses in the fracture process zone [6, 7]. These give rise to a reduced macroscopic toughness for perpendicular and enhanced fracture toughness for parallel cracks. The domain switching at crack tips induced by mechanical or electric loading has been studied by using scanning electron microscopy and X-ray technique in [8, 9]. According to [10, 11], an additional electric loading changes the anisotropic ratio, making the crack in the perpendicular direction longer under positive electric field or shorter under negative electric field, however, having very little influence on the crack length in the parallel direction. While [10] relies on Vickers indentation tests, in [11] compact tension specimens have been used. The same effect of the electric loading on the crack growth in the perpendicular direction was observed in [12]. However, a reverse observation has been reported in [13], again with Vickers indentations. Further experiments [6, 14, 15], came to the conclusion that, applying a large indentation load, both positive and negative electric fields reduce the fracture toughness, no matter if applied parallel or perpendicular to the crack. Crack growth driven by pure cyclic electric loading of different magnitudes in PZT and lead lanthanum zirconate titanate (PLZT) was investigated experimentally and theoretically explained in [16, 17] and further in [18] a mechanical loading was superimposed.

35 Many other individual factors in ferroelectrics can affect the fracture behavior and have thus been investigated. The permittivity of the crack interior has an influence which was observed e.g. in [19], where $\varepsilon = 40\varepsilon_0$ (ε_0 : dielectric constant of vacuum) was determined as an equivalent dielectric constant. Some other papers have the same focus [20, 21]. Influences of grain size and three different poling directions on the crack resistance curve (R-curve) were discussed in [22, 23], whereupon the
40 toughening effect increases with the grain size and a poling parallel to the crack front exhibits the largest fracture toughness all along the R-curve. In [24, 25] R-curves are presented, which have been measured with DCB specimens under pure mechanical and combined electromechanical loading along the poling direction, being perpendicular to the crack. The experiments reveal that a positive electric field above the coercive field shifts the R-curve to larger values of the fracture toughness.
45 Additionally, environmental effects, e.g. temperature and humidity, influence the fracture behavior of ferroelectrics [26, 27]. Furthermore, a temperature rise promotes domain switching and vice versa, particularly in the vicinity of the crack tip, leading to unstable crack propagation [28]. Some review papers provide a comprehensive overview on experiments in ferroelectrics [29, 30, 31].

Different theoretical analyses, e.g. [32, 33], have been established to explain the experimental
50 observations. New fracture criteria, modified for ferroelectrics, were proposed and experimentally validated [11, 12]. Especially, the mechanical and electric energy release rates were discussed in this context [6, 21]. Analogous to the classical Dugdale-model, a strip saturation model has been developed, comparing the local and global energy release rates [34]. This model takes advantage of the fact that, to a certain extent, the electric displacement and the electric field phenomenologically
55 play similar roles as stress and strain. A similar model, the strip dielectric breakdown model, was proposed in [35], where instead of polarization the electric field strength saturates in front of the physical crack tip, since the local electric field is much larger than the dielectric breakdown strength there. A wedge model based on the mechanical strain energy release rate was developed, providing results being in good agreement with experiments [36]. Numerical results based on different fracture
60 criteria and models were compared to the experimental outcomes in [12].

Crack paths in ferroelectrics, however, have been rarely investigated. One of the probably most essential experimental works is presented in [11], where a three-point bending PZT-4 specimen with an eccentric notch position was employed for attaining a curved crack path under mechanical mixed mode loading and an electric field. Unfortunately, results of just one single specimen per notch po-
65 sition are included in [11]. A comparison with crack paths under different electric loading conditions

or repeated experiments providing data for a statistical analysis are missing. A solid conclusion about the influence of electric fields on crack deflection is thus not given. Nevertheless, the crack path in [11] has served as a reference for a few numerical simulations. In [37] finite element (FE) simulations with linear piezoelectric constitutive behavior and adaptive remeshing provide crack paths for different notch positions. The boundary element method and also a linear constitutive model in [38] yield similar results, providing just a rough accordance with the experimental crack paths from [11]. In both works the anisotropy of fracture toughness is taken into account in a simplified manner, assuming a homogeneous polarization in the fracture process zone. A nonlinearity in front of the crack tip is considered in [39], whereupon the experimental crack path in [11] is well reproduced, if a calibration parameter of the saturation strip model is appropriately chosen. In all these simulations, the maximum hoop stress has been employed to predict crack deflection angles, scarcely being influenced by electric fields, thus providing crack paths depending on the mechanical load only. In [40], on the other hand, an energy density criterion has been applied to predict crack deflection in an infinite piezoelectric plate under mixed-mode loading, giving insight into the influence of electric fields. A different work [41] presents the crack paths in PZT ceramics driven by cyclic electric loading both experimentally and numerically, primarily studying the influence of the width of the electrodes on the crack paths.

One goal of this work is to provide statistically evaluated results of experimental crack paths in PZT, investigating the influence of both positive and negative electric fields below E_c on the crack deflection. Different specimen and loading configurations were critically reflected prior to the experiments, with the goals to obtain curved crack paths under pure mechanical loading on the one hand side and to efficiently impose an electric field on the other. The non-symmetric three-point bending setup according to [11] finally appeared to provide the most favourable conditions. In contrast to [11], PZT-5H was used instead of PZT-4, after all allowing at least a qualitative comparison of the results. To obtain sufficiently many crack paths for a statistical evaluation with three different electric loading regimes, just one single position of the notch has been introduced. One experiment at pure mechanical loading has been recorded with a high speed camera, providing remarkable details on the onset and propagation of a crack in a ferroelectric ceramic. Linear piezoelectric FE simulations under different electric loading conditions based on both hoop stress and a new modified J -integral deflection criterion reveal crack paths, matching the actual experimental findings better than those in [11], particularly in an early stage of growth.

2. Experimental set-up and testing procedure

Fig. 1 shows the geometry of the three-point bending specimens. The piezoelectric plates (PZT-5H, provided by the Institute of Acoustics, Chinese Academy of Sciences) of dimensions $19.1 \times 9 \times 5.1$ mm, with an average grain size of $4 \mu\text{m}$, were poled in silicon oil in order to avoid flashovers. An electric field of 3000 V/mm ($E_c = 700 \text{ V/mm}$) was applied along the longest edge of the un-notched specimen to obtain a homogeneous polarization state. The material constants of polarized PZT-5H are listed in Appendix A. The left and right surfaces of the specimens are coated with silver electrodes, which were sintered at $700 \text{ }^\circ\text{C}$. The poling direction is from left to right, see Fig. 1. The off-center notch, with a width of about 0.7 mm and a depth of approx. 3.7 mm , is perpendicular to the poling direction and was cut by a wheel cutter and subsequently polished. At the root of the primary notch, a thin slit was subsequently introduced by using a surgical scalpel of 0.1 mm thickness in order to facilitate crack initiation. The total final length of the sharpened notch is 4 mm . A photograph of two specimens is shown in Fig. 2.

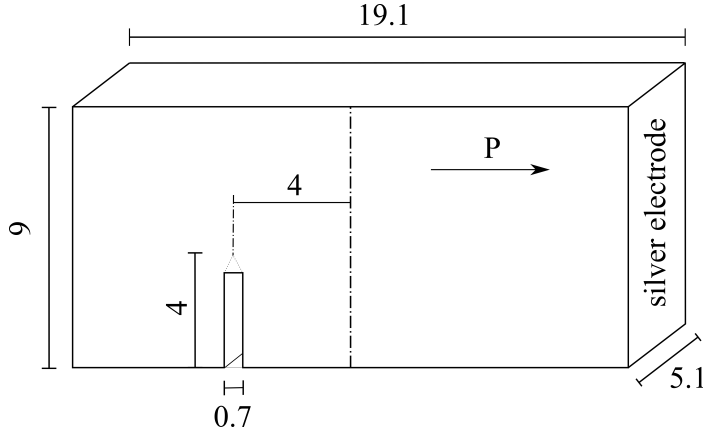


Fig. 1: Specimen for the electric-mechanical mixed mode fracture test (units in mm). The thin dotted lines at the root of the primary notch indicate the sharpened notch tip.

During the experiments involving an electric field, the specimens were placed in an acrylic glass container filled with silicon oil for insulation. A constant voltage of 10 kV was generated by a Trek Model 10/40A-HS amplifier, corresponding to $E = \pm 0.75 E_c$ for PZT-5H. The wires connecting the amplifier's outputs and the silver electrodes on the specimens were glued on the electrode surfaces with an electrically conducting polyurethane adhesive (PU 1000, Polytec PT) hardening at room

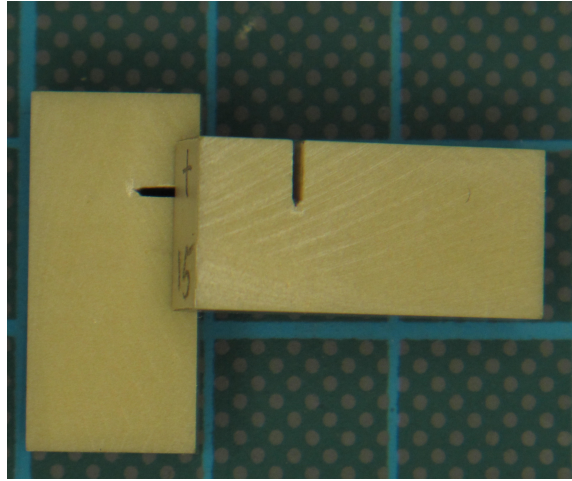


Fig. 2: Two prepared specimens with notches.

115 temperature.

The force controlled mechanical loading was generated by a double-acting pneumatic cylinder, where the piston rod is powered by compressed air pumped into the cylinder from the upper port, thus moving downwards. The piston rod transfers constant force for any position, if the air pressure remains constant. The circular effective area of the cylinder has a diameter of 25 mm. The mapping
120 between the pressure gauge and the force has been calibrated, see Fig. 3. The estimated critical fracture load is larger than 120 N, corresponding to approx. 2.5 bar, where the error is smaller than 1%. The schematic arrangement of the whole experimental set-up and a photograph of the mechanical loading unit are shown in Fig. 4. Fig. 5(a) illustrates the mechanical loading procedure without applied electric field and Fig. 5(b) shows the broken specimen at the end of the experiment.

125

3. Experimental results

3.1. General observations of crack growth under pure mechanical loading

Since crack growth in the force-controlled three-point bending test is unstable, the crack length is not controllable and a critical loading instantaneously leads to spontaneous failure. The crack
130 velocity, however, is much lower than typical velocities of surface waves in elastic ceramic materials. Crack propagation has been recorded by a high-speed camera for one of the tests without electric

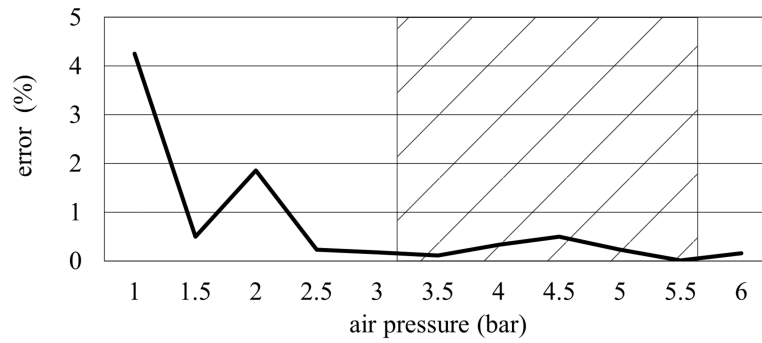
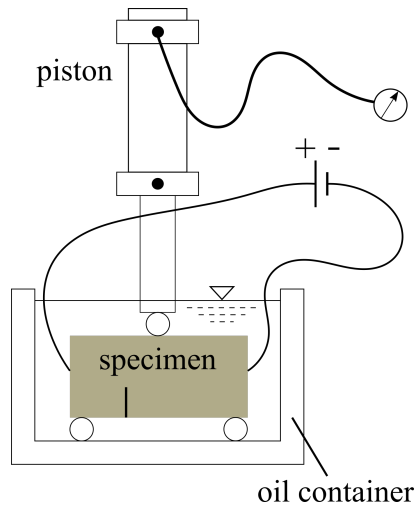
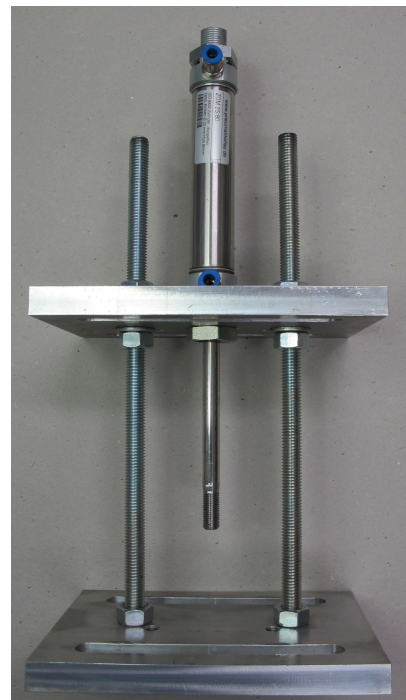


Fig. 3: Calibration of the applied force, where the error of measuring the force with a pressure gauge is given and the hatched area indicates the range of operation.



(a)



(b)

Fig. 4: (a) Working principle of three-point bending test, (b) loading frame for the mechanical force.

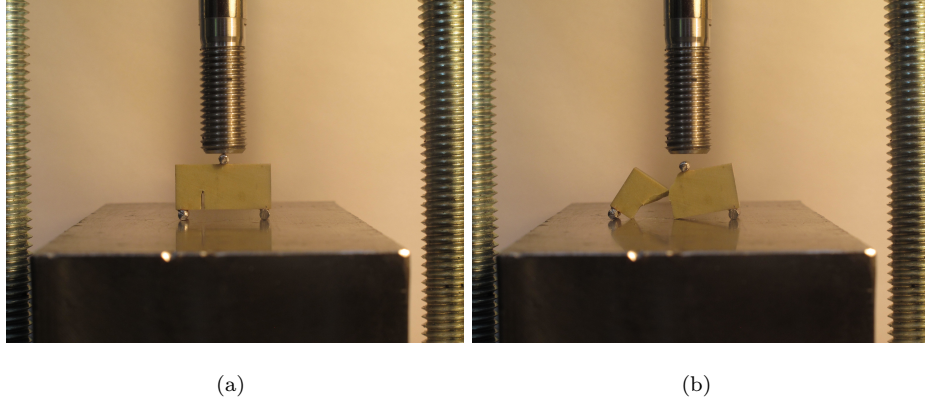


Fig. 5: Specimen without electric loading and (a) piston rod with a remaining 1 mm stroke length, (b) spontaneously broken specimen after critical load has been attained.

loading. The high-speed camera recorded 65100 frames per second, six of them have been selected in Fig. 6.

It is remarkable that before the crack starts to initiate and propagate from the sharpened notch tip, which is supposed to take place as soon as the mechanical load is sufficiently large, a short white line is formed, see Fig. 6(b) where it is denoted as pre-fracture line. After its instantaneous appearance it is arrested for about 0.3 s, then it continues growing rapidly towards the upper boundary of the specimen, see Fig. 6(c). Immediately following that, the actual crack initiates, and the subsequent crack path exactly follows the white line, see Fig. 6(d)-(f). The whole process of crack growth takes about 1.5×10^{-4} s, whereupon an average propagation speed of 42 m/s is identified.

However, it is not clear how the observed white line comes up and what it essentially is. It reminds of localization or shear bands which, however, are in fact only known from ductile [42] or quasi-brittle materials, exhibiting a pronounced strain softening behavior before failure. Just after the localization band shows up, the deformation results in damage and cracking in this narrow zone. The appearance of localization bands is akin to what is observed in Fig. 6, even though the PZT ceramic is commonly known as a brittle material. On the other hand, ferroelectric/-elastic domain switching incorporates a pronounced nonlinearity, taking the inelastic part of deformation just as plasticity in ductile materials.

In order to further illuminate that feature, the stress vectors on the pre-fracture line were

computed with linear piezoelectric finite elements and illustrated in Fig. 7. The pre-fracture line considered in the calculation has been extracted and averaged from different experimental results of crack paths under the same boundary and loading conditions. The longer stress vectors (blue) on the pre-fracture line in Fig. 7 are almost either parallel or anti-parallel to the normal directions indicated by the black arrows of unit length. Near the notch tip normal stresses are tensile, while at the last three sampling points they are compressive. The directions of the stress vectors turn around gradually along the pre-fracture line. Their magnitudes are first reduced, increasing again after the change from tensile to compressive. Due to the singularity, the stress near the notch tip, which has been modeled as crack tip, is much larger than elsewhere. In the upper part, stress vectors will rotate further in the vertical direction due to the compressive stress near the point of loading which is not included in the figure. According to Fig. 7 the pre-fracture line is essentially oriented perpendicular to the directions of the stress vectors, thus it is exposed to principal tensile or compressive stress rather than to shear stress as is known from classical localization bands in ductile materials. The point of transition from tensile to compressive stress seems to correspond to the tip of the pre-fracture line in Fig. 6(b), where it has been arrested for 0.3 seconds.

Further insight into the nature of the pre-fracture or localization line could be expected by Digital Image Correlation (DIC) measurements on the surface of a loaded specimen. In-situ measurements, however, appear to be a challenging task, since the required frame rate of a high speed recording and an appropriate image resolution are competing aspects. The application of a sufficiently fine stochastic speckle pattern on the comparatively small test surface is considered to be challenging too. A promising approach to the shed light on the nature of the pre-fracture line in Fig. 6 could be a numerical simulation of the experiment based on nonlinear ferroelectric constitutive behavior.

High speed recordings of experiments with electric loads are not possible with the employed experimental set-up. The limiting factor is the required power density of the illumination system, depending linearly on the recording frame rate. The extraordinarily powerful spotlight used for the images of Fig. 6 does not provide enough light if the specimen has to be immersed into an oil-filled acrylic glass box. Whether the phenomenon of a pre-fracture line prevails under combined electromechanical loading thus remains unanswered.

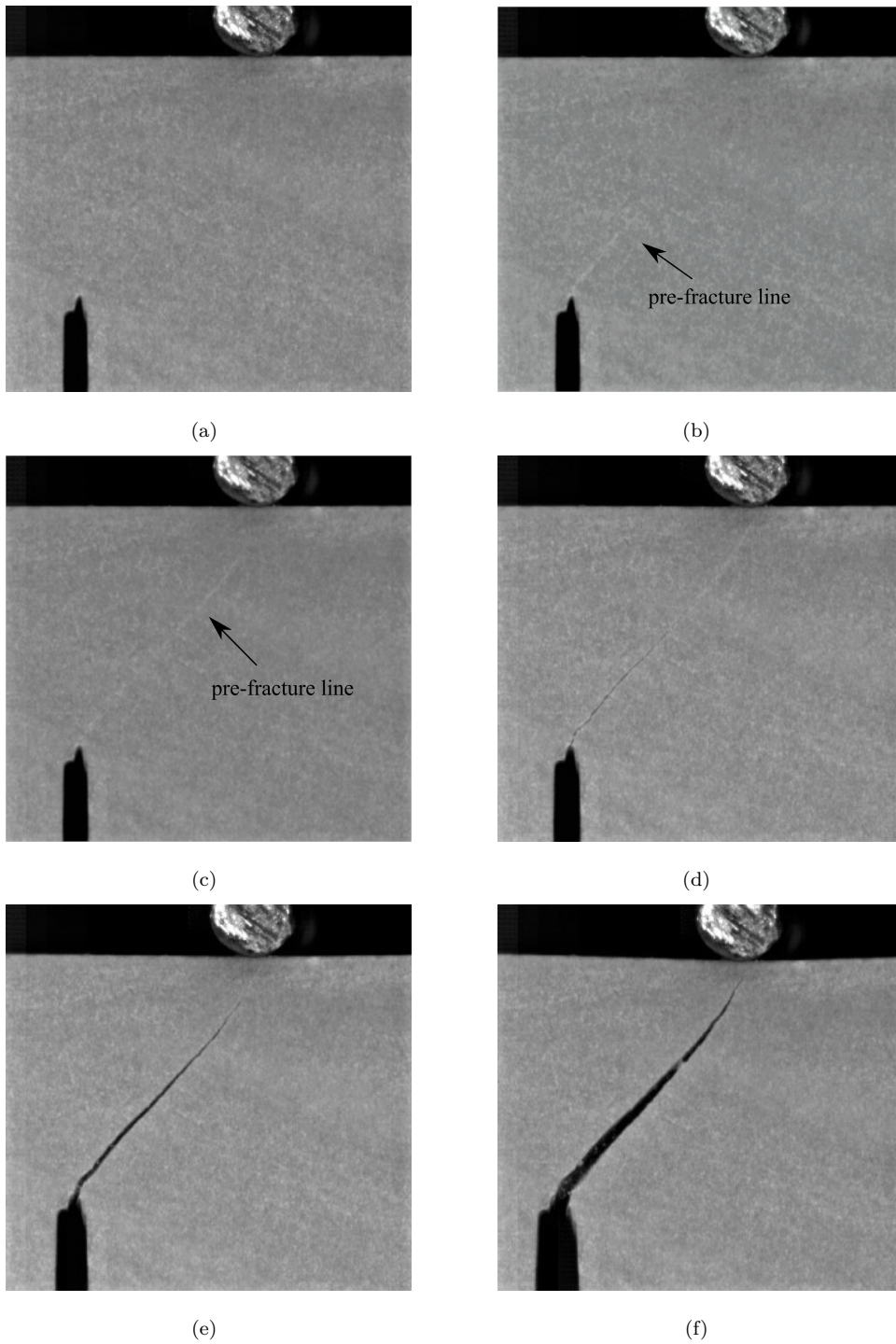


Fig. 6: Stages of a high-speed recording of pure mechanical loading: (a) loaded specimen prior to localization or cracking, (b) increasing the applied force a white line appears in front of the notch tip, (c) after a 0.3 s arrest the white line continues propagating, (d)-(f) a crack initiates and propagates along the white line.

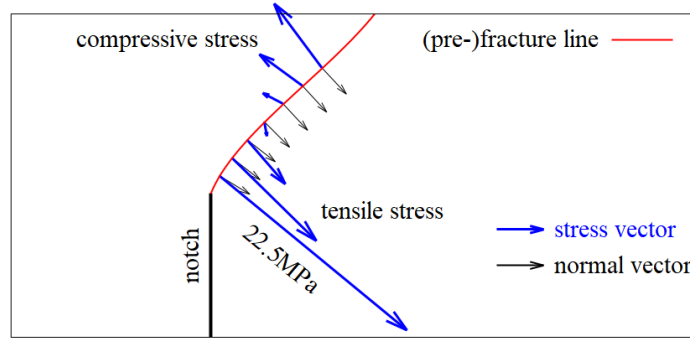


Fig. 7: Normal vectors (thin black) and calculated tensile and compressive stress vectors (thick blue) at selected points on the pre-fracture line, which has been scanned and averaged from crack paths of all specimens under identical (pure mechanical) loading conditions. The averaged critical load of 272.4 N was applied in the simulation as a single force.

3.2. Comparison of the crack paths under different loading conditions

180 Three different loading cases were tested, i.e., mechanical load without electric field and mechanical load with electric field parallel or anti-parallel with respect to the direction of polarization. For each loading condition, five specimens have been tested. A high-resolution scanner was used to scan the specimens and the crack paths were extracted from the pictures. All the crack paths of the 15 tests are illustrated in Fig. 8 and the averaged paths based on five tests of each case with error bars are shown in Fig. 9.

The results show clearly that the crack under pure mechanical loading propagates with the largest deflection angle. Electric fields, in both parallel and anti-parallel directions, reduce the deflection, however to different extents. This tendency is confirmed by the critical mechanical loads of crack initiation, where averaged values 272.4 N, 249 N and 200.7 N correspond to $E = 0$, $E = 0.75E_c$ and $E = -0.75E_c$, respectively. In Tab. B.1 all fracture forces are given for the individual specimens. The electric field in anti-parallel direction ($E = -0.75E_c$) leads to the least deflection and is coming up with the largest scattering, being manifested in the longest error bars. The reason for that probably is the domain switching near the crack tip. The electric load is selected such that the electric field is large enough to have influence on the fracture behavior, however will not exceed the coercive field, which means that the general polarization state of the specimens will not be changed. Nevertheless, close to the crack tip the electric field is definitely beyond the

switching barrier, thus inducing domain switching, predominantly for negative electric fields. The latter makes the fracture process more unstable and promotes the diversity of the crack paths.

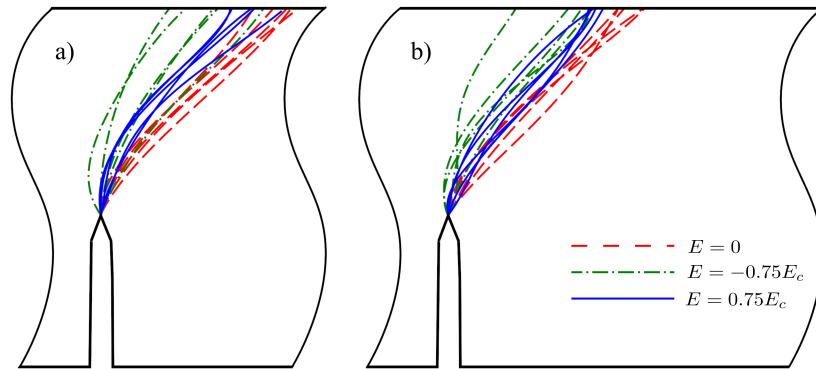


Fig. 8: Crack paths of three-point bending tests under different electric loading conditions, (a) view from the front sides and (b) view from the back sides of the specimens.

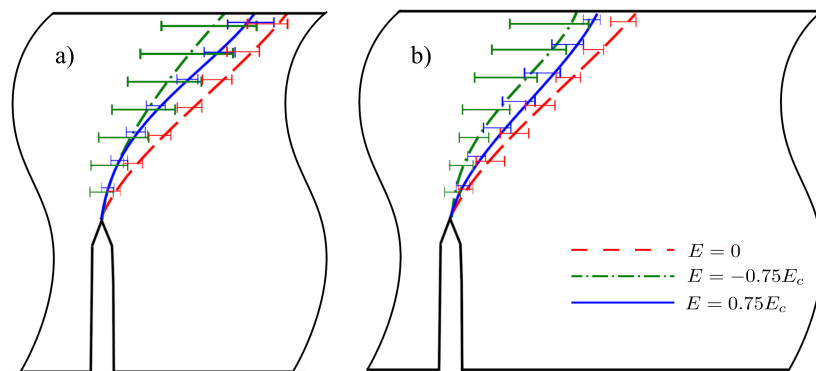


Fig. 9: The crack paths averaged from five tests for each electric loading condition and associated error bars: (a) view from the front side, (b) view from the back side of the specimen.

Although not all the details of the three-point bending test in this work are comparable to the
 200 experiment in [11], e.g., the employed material (PZT-5H vs. PZT-4) and the applied electric field

($0.75E_c$ vs. $0.33E_c$ ¹), the crack paths are compared qualitatively. Since only one single path for the chosen notch position is available in [11], which was driven under positive electric field, the current results of $E = 0.75E_c$ are taken for comparison. Fig. 10 shows the averaged crack paths from the front and back sides of our experiments, having similar deflection angles at the initiation point and being close to each other during crack growth. In contrast, the crack path from [11] deflects to the left side of the notch, continuing with a path which is distinctly more curved than the ones from the current experiments.

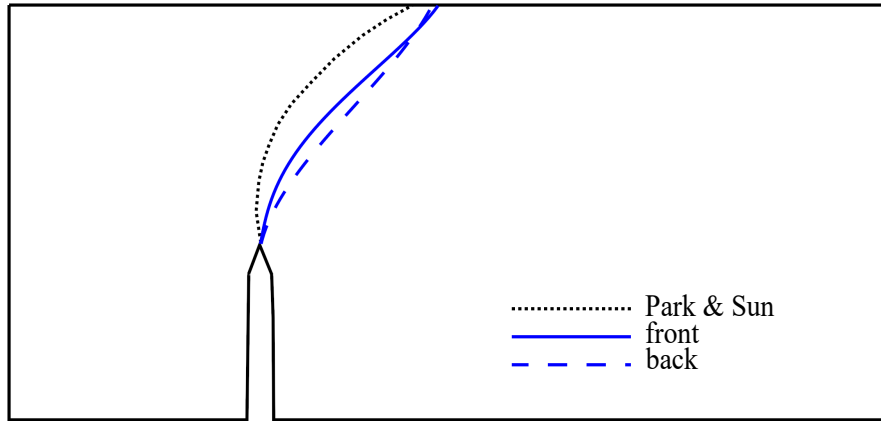


Fig. 10: The averaged crack paths for $E = 0.75E_c$ on both sides of PZT-5H specimens from the current experiments and the crack path from [11].

4. Simulation of crack growth

Just as in [37, 38, 39, 40] crack paths in the ferroelectric material are investigated numerically based on a linear piezoelectric constitutive framework in connection with classical crack deflection criteria in brittle solids, adapted to the feature of electromechanical coupling. The J -integral criterion based on the concept of configurational forces is modified in this context, providing a new deflection criterion, basically being valid in both elastic and inelastic materials. Crack path simulations accounting for nonlinear ferroelectric constitutive behavior in the whole specimen are still

¹The ratio of the applied electric field and the coercive field is not given in [11]. E_c of PZT-4 depending on different factors, a common value from [43] is taken here.

215 not state of the art nowadays, except for simulations of straight mode-I cracks without deflection. A fully nonlinear simulation is required if the whole process of crack growth, including the observed pre-fracture line, see Fig. 6, is to be investigated numerically. Concerning the predicted crack path itself, a linear piezoelectric calculation of the specimen is certainly appropriate. The experiments outlined in Sect. 3 and [11] are taken as a basis for comparison with the simulations.

220 4.1. Crack tip loading and classical deflection criteria

Within the framework of linear piezoelectric fracture mechanics, closed form solutions of stress and electric displacement have been derived, see e.g. [44], where an additional field intensity factor K_{IV} for the electric displacement field is introduced akin to the conventional stress intensity factors K_I , K_{II} and K_{III} , representing the electric flux singularity in front of the crack tip. The crack in this work is considered as impermeable, whereupon its interior has zero dielectric permittivity. Applying the generalized crack closure integral [25], the energy release rate is related to the field intensity factors as follows

$$\begin{aligned}
 G &= \lim_{\Delta a \rightarrow 0} \frac{1}{2\Delta a} \int_0^{\Delta a} [\sigma_{i2}(r)\Delta u_i(\Delta a - r) + D_2(r)\Delta\varphi(\Delta a - r)] dr \\
 &= \frac{1}{2}K_i Y_{ij} K_j, \quad i, j = 1, 2, 3 \text{ represent mode-II, I, IV,}
 \end{aligned}
 \tag{1}$$

where Y_{ij} is the Irwin matrix of piezoelectric materials, see Appendix A, and the anti-plane shear mode-III has been omitted for plane crack problems. In Eq. (1) r is the distance from the crack tip and Δa is the crack growth increment. The stress σ_{i2} , electric displacement D_2 , crack opening displacement Δu_i and electric potential jump $\Delta\varphi$ are taken from asymptotic near tip solutions [25] of the ligament and the crack surfaces, respectively. Expanding Eq. (1) for a crack being perpendicular to the poling direction, the following relation is obtained:

$$G = \frac{1}{2}Y_{22}K_I^2 + \frac{1}{2}Y_{11}K_{II}^2 + \frac{1}{2}Y_{33}K_{IV}^2 + Y_{23}K_I K_{IV}.
 \tag{2}$$

Confining the crack closure to the mechanical work, the total electric-mechanical energy release rate G is degenerated as mechanical energy release rate

$$G^m = \lim_{\Delta a \rightarrow 0} \frac{1}{2\Delta a} \int_0^{\Delta a} \sigma_{i2}(r)\Delta u_i(\Delta a - r)dr = \frac{1}{2}Y_{22}K_I^2 + \frac{1}{2}Y_{11}K_{II}^2 + \frac{1}{2}Y_{23}K_I K_{IV}.
 \tag{3}$$

Crack growth and rupture of material, respectively, being a mechanical process, may justify to consider G^m in a fracture criterion for piezoelectric materials [11, 12, 24]. The electric field, in this case, is supposed to have an impact exclusively due to the piezoelectric coupling effect.

A second energy term H is defined by formally replacing σ_{i2} by σ_{i1} and D_2 by D_1 in Eq. (1):

$$\begin{aligned} H &= \lim_{\Delta a \rightarrow 0} \frac{1}{2\Delta a} \int_0^{\Delta a} [\sigma_{i1}(r)\Delta u_i(\Delta a - r) + D_1(r)\Delta\varphi(\Delta a - r)] dr \\ &= -\frac{1}{2}K_i S_{ij} Y_{jk} K_k, \end{aligned} \quad (4)$$

where S_{ij} is a characteristic matrix only depending on the material constants, see Appendix A.

The coordinates of the path independent J -integral [33]

$$J_k = \oint_{\Gamma} (\Pi n_k - \sigma_{ij} n_j u_{i,k} - D_j n_j \varphi_{,k}) d\Gamma, \quad (5)$$

with

$$\Pi = \frac{1}{2}(\sigma_{ij}\varepsilon_{ij} - D_i E_i) \quad (6)$$

as electric enthalpy density, the strain ε_{ij} , the electric field $E_i = -\varphi_{,i}$ and the unit normal n_j of the closed integration contour Γ , are related to the total energy release rate and the quantity H according to Eq. (4) as [45]

$$J_1 = G, \quad J_2 = -H. \quad (7)$$

For determining the deflection angle $\bar{\theta}$ of the crack, the J -vector criterion [46, 47, 48] is adopted amongst others. It predicts that for isotropic materials the crack grows in the direction of the J -vector, thus leading to a maximum energy release of the structure, i.e.

$$\bar{\theta} = \arctan\left(\frac{J_2}{J_1}\right) = \arctan\left(\frac{-H}{G}\right). \quad (8)$$

225 One advantage of the J -vector criterion is i.a. that anisotropic material behavior is easily incorporated [47, 48], not requiring the anisotropic eigenfunctions of the Williams series. Further, the criterion has been successfully validated based on experimental results in classical structural materials of differently pronounced anisotropy ratios [47, 48]. In Eq. (8), H and G have been introduced following Eq. (7), whereupon the deflection angle $\bar{\theta}$ can be determined from field intensity factors
230 accounting for Eqs. (2) and (4).

Another crack deflection criterion, also employed in this work for comparison, is the maximal hoop stress criterion, which proved to be a reliable criterion for classic structural materials [49].

Accordingly, the crack grows into the direction $\bar{\theta}$ where the hoop stress $\sigma_{\theta\theta}$ has its maximum value, i.e.

$$\left. \frac{\partial \sigma_{\theta\theta}}{\partial \theta} \right|_{\theta=\bar{\theta}} = 0, \quad \left. \frac{\partial^2 \sigma_{\theta\theta}}{\partial \theta^2} \right|_{\theta=\bar{\theta}} < 0. \quad (9)$$

For piezoelectric materials, the stress and thus the deflection angle in principle depend on the electric field, although numerical studies reveal a vanishing impact on $\bar{\theta}$ predicted by the criterion Eq. (9). Just as in the modified J -integral criterion, introduced in the following section, it is an indirect dependence, focusing on a mechanical quantity controlling fracture.

235 4.2. Modified J -integral criterion of crack deflection

Motivated by one common approach to piezoelectric fracture, supported by various works [11, 12, 24], where the electric contribution is neglected in the energy release rate, see Eq. (3), the J -integral deflection criterion shall be modified likewise. Unlike the energy release rate, where a separation of electrical and mechanical parts is straightforward, the related modification of the J -integral requires some physical interpretation. Consider the change of the specific potential $\delta\Pi$ due to a reversible virtual work δW_{rev} and a dissipative work δW_{diss} , i.e.

$$\delta\Pi = \delta W_{rev} + \delta W_{diss} = \delta W_{rev}^m + \delta W_{rev}^e + \delta W_{diss}, \quad (10)$$

where δW_{rev} is separated into a mechanical and an electrical part, δW_{rev}^m and δW_{rev}^e , respectively. A configurational force F_k in terms of a thermodynamic driving force is introduced next [50], whose virtual work due to an irreversible virtual displacement δz_k of any kind of a defect is related to the dissipative part of Eq. (10), thus leading to

$$F_k \delta z_k = \int_V \delta W_{diss} dV = \int_V (\delta\Pi - \delta W_{rev}^m - \delta W_{rev}^e) dV. \quad (11)$$

The defect is entirely enclosed by the boundary of a domain V . A more classical interpretation of the driving force is obtained by alternatively introducing the irreversible entropy production δS_{irr} in the energy balance Eq. (10) yielding

$$\delta\Pi = \delta W_{rev} + T \delta S_{irr}, \quad (12)$$

where the exchange entropy due to heat transfer $T \delta S_{ex}$ has been disregarded and T is the absolute thermodynamic temperature. It is obvious from Eqs. (10) to (12) that

$$F_k \delta z_k = \int_V T \delta S_{irr} dV, \quad (13)$$

whereupon the configurational force is related to the entropy production at defect displacement.

Inserting $\delta W_{rev}^m = \sigma_{ij}\delta\epsilon_{ij}$ and $\delta W_{rev}^e = -D_i\delta E_i$ into Eq. (11) and applying the relation $\delta\psi = \psi_{,k}\delta z_k$ to any of the quantities $\psi = \epsilon_{ij}, E_i, \Pi$ changed by virtual defect displacement δz_k , allows for the calculation of the configurational force according to

$$F_k = \int_V (\Pi_{,k} - \sigma_{ij}u_{i,jk} - D_i\varphi_{,ik}) dV, \quad (14)$$

where the discrete displacement δz_k has been deleted on both sides and the displacement gradient $u_{i,j} = 2\epsilon_{ij} - u_{j,i}$ as well as the electric potential φ have been introduced.

Separating the specific potential energy $\Pi = \Pi^m + \Pi^e$ into mechanical ($\Pi^m = \sigma_{ij}\epsilon_{ij}/2$) and electric ($\Pi^e = -D_i E_i/2$) parts, the configurational force is divided into electric and mechanical contributions:

$$F_k = F_k^m + F_k^e = \int_V (\Pi_{,k}^m - \sigma_{ij}u_{i,jk}) dV + \int_V (\Pi_{,k}^e - D_i\varphi_{,ik}) dV. \quad (15)$$

Disregarding inertia and other volumetric forces, applying Gauss' integral theorem and introducing tractions $t_i = \sigma_{ij}n_j$, the mechanical driving force of Eq. (15) finally reads

$$F_k^m = J_k^m = \oint_{\Gamma} (\Pi^m n_k - t_i u_{i,k}) d\Gamma, \quad (16)$$

where F_k is replaced by J_k for crack-like defects. Eq. (16) is obtained from Eq. (5) by deleting the
240 electric quantities.

The J -integral is related to the energy release rate via the reduction of total potential energy δU , in a plane structure of unit thickness due to virtual crack growth δa :

$$\delta U = -J_k \delta z_k = -(J_k^m + J_k^e) \delta z_k = -G \delta a = -(G^m + G^e) \delta a, \quad (17)$$

where $\delta z_k = z_k \delta a$ with $z_k z_k = 1$. Taking into account Eq. (13), the mechanical contribution of the J -integral and configurational force, respectively, gives rise to one part of entropy production δS_{irr}^m , being attributed to the mechanical process of crack growth.

A modified J -integral criterion based on J_k^m can thus be formulated for isotropic materials as follows:

$$\bar{\theta} = \arctan\left(\frac{J_2^m}{J_1^m}\right). \quad (18)$$

It postulates that the crack deflects into the direction of the mechanical part of the driving force and maximum release of potential mechanical energy, respectively. In contrast to Eq. (8), where J_1 and J_2 are related to G and H , an analogous relation is not given for Eq. (18), since $J_1^m \neq G^m$ and $J_2^m \neq -H^m$, where H^m could be defined in the style of Eqs. (3) and (4). The basic advantage of applying H and G is that the J -integral vector can be calculated without any contour or equivalent domain integral, just by applying Eqs. (2) and (4). Piezoelectric anisotropy is taken into account in the criteria Eqs. (8) and (18), however a directional variation of crack resistance requires a modification [47].

4.3. Numerical results of crack paths

Finite element (FE) analysis is adopted to simulate crack growth. Eight-node rectangular elements with quadratic shape functions are employed in the FE software Abaqus. The elements around the crack tip are distorted into irregular triangular elements, where the middle nodes on the collapsed element edges are shifted into the quarter positions near the crack tip [25, 51]. With the crack tip element method (CTEM) applied in a post-processing, the field intensity factors are accurately calculated from nodal crack face displacements and electric potentials within the irregular elements.

The deflection of the crack is determined by the three criteria introduced in Sects. 4.1 and 4.2. The intensity factors K_I , K_{II} , K_{IV} from the CTEM are inserted into Eqs. (2) and (4) for the classical J -integral criterion Eq. (8), and are the basis of the hoop stress criterion Eq. (9), where $\sigma_{\theta\theta}(K_i)$ is taken from the piezoelectric crack tip near field [25, 38]. The modified J_k^m -criterion of Eq. (18) requires the calculation of a contour integral according to Eq. (16).

A smart adaptive re-meshing algorithm has been developed for simulating crack growth [52]. For every crack growth increment the new crack tip is shifted in the predicted deflection direction and the whole model is meshed again. The crack increment length is chosen sufficiently small to provide convergence in the crack paths. The constitutive framework adopts linear piezoelectricity and infinitely small deformations are further assumed. An anisotropy of crack resistance is neglected.

The different numerical results are compared in Fig. 11. At first glance, the crack paths based on the maximum hoop stress criterion do not depend on the electric load at all. A closer look in terms of a magnification, however, reveals that the results are slightly different. The angular functions of the near tip limit of the electromechanical crack solution not depending on the electric field [25], K_I ,

K_{II} vs. K_{IV} are the weights of the mechanical and electrical contributions to $\sigma_{\theta\theta}$. K_{IV} , typically
 275 being in the order of $10^{-3} \text{ Cm}^{-3/2}$, thus gives rise to a ratio of electric to mechanical contributions of
 not more than $10^{-2} - 10^{-3}$. The crack path from the hoop stress criterion shows a larger deflection
 from the notch than the one predicted by the J_k^m -criterion of Eq. (18) for a positive electric field.
 Another crack path in point dashed line, which is determined by the J_k -criterion based on the total
 electromechanical energy according to Eq. (8), provides non-physical results. Therefore, based
 280 on the present comparison, just the maximum hoop stress and the J_k^m -criterion seem to at least
 qualitatively reproduce the experimental paths.

Looking closer at the crack paths of the J_k^m -criterion in Fig. 11(b), positive electric loading
 reduces crack deflection, basically agreeing with the experimental results in Fig. 9, both qualita-
 tively and quantitatively concerning the relative amount of reduction. The green dash-dotted line
 285 corresponding to the negative electric load, however, enhances the crack deflection in contrast to
 the experiment in Fig. 9, where a reduction of deflection is observed. In [40] our predictions are
 qualitatively confirmed, based on an energy density deflection criterion and the model of a crack in
 an infinite piezoelectric plate under Mode-I/II/IV loading.

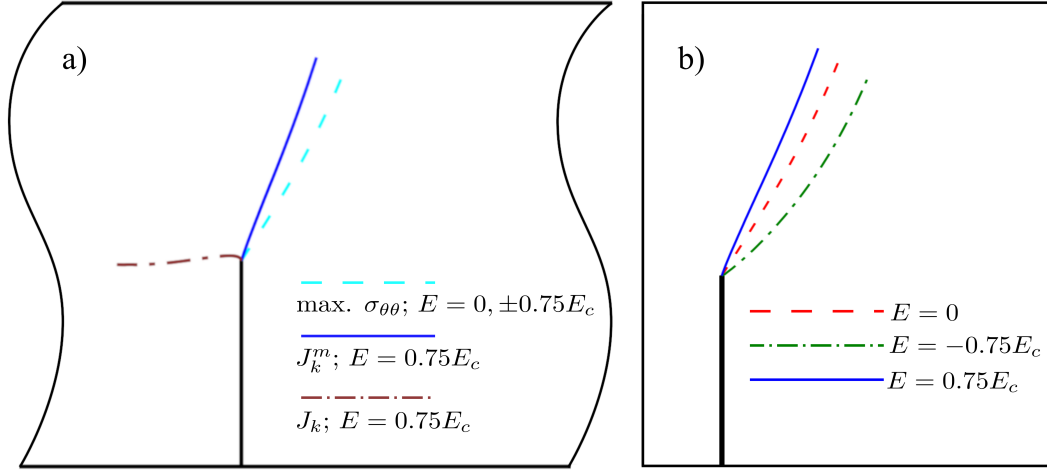


Fig. 11: (a): the calculated crack paths for critical mechanical loads measured from the experiment under various electric loading conditions and deflection criteria and (b): comparison of electric loads for the J_k^m -criterion Eq. (18) with three types of electric loading.

The crack paths of the simulation applying the J_k^m -criterion are compared to the experimental findings with $E = 0.75E_c$ in Fig. 12, where the averaged paths of front and back sides of the specimens have been taken from Fig. 10. The three curves show similar initial kinking angles and continue propagating in the same direction. The curvatures of the experimental paths, however, are larger than the one from the simulation, thus increasing their divergence at further growth.

The deficiency of simulation and experiment, although fundamentally smaller than from comparisons of linear piezoelectric calculations and the data in [11], is supposed to be mainly due to two aspects which have been disregarded in the model. First of all, ferroelectricity and -elasticity, giving rise to nonlinear phenomena in a crack tip process zone, will lead to inelastic stress and polarization switching. In particular, switching-induced shear stress might effectuate a non-negligible contribution to crack deflection. Even more important, however related to this issue, might be the impact of fracture toughness anisotropy of ferroelectrics, which was demonstrated to be considerable, e.g. by Vickers indentation experiments [6, 10, 13]. The associated influence on the curvature of cracks and even qualitative features of crack paths was shown to be crucial in [47, 48], where smaller anisotropy ratios of rolled aluminum alloy and larger ratios in short fibre reinforced polymer matrix composites were investigated. Though in [37] and [38] anisotropy of crack resistance has been considered in principle, local polarization reorientation has been neglected, assuming a constant polarization and axis of anisotropy, respectively, in the whole specimen. Especially for the negative electric field, however, Fig. 9 due to longer error bars illustrates the significance of domain switching in this electric load case, exhibiting the most prominent discrepancy of crack paths in Figs. 9 and 11(b). Apart from that, the maximum hoop stress criterion employed in [37] and [38] is not suitable for investigating the influence of electric fields on crack paths, see Fig. 11(a).

5. Conclusions

Three-point bending tests with single edge-notched poled piezoelectric PZT-5H specimens have been reported, where the mechanical load has been superimposed with electrical loads in two opposite directions with intensities below the coercive field. The eccentric position of the notch leads to curved crack paths, even without electric loading. Several tests have been made with each electromechanical loading set-up, in order to investigate the scattering of the crack paths. The latter differ fundamentally from former investigations in the 1990s, which have hitherto been taken as a reference for numerical crack path predictions in piezoelectrics.

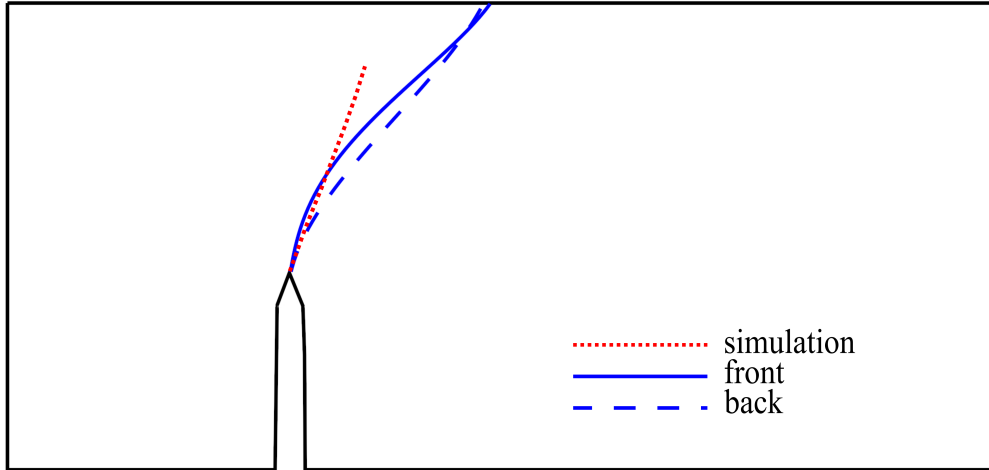


Fig. 12: Comparison of the crack paths from simulation applying the J_k^m -criterion and experiment with averaged paths on front and back surfaces of the specimens for $E = 0.75E_c$.

The averaged paths turn out to be influenced by the electric loading in such a way that both
 320 positive and negative electric fields reduce the crack deflection, whereupon negative fields exhibit the
 largest scatter, probably due to enhanced domain switching, and the least deflection from the notch
 plane. Numerical simulations based on a linear piezoelectric material model have been carried out
 in connection with different crack deflection criteria. A new deflection criterion has been suggested,
 modifying the J -vector criterion by focusing on mechanical energy contributions. In contrast to the
 325 maximum hoop stress criterion, the modified J -vector criterion predicts distinctly different crack
 paths depending on the electric field. While the influence of a positive field is predicted reasonably,
 for a negative field much larger deflection is obtained than in the experiment.

Particularly the predicted initial deflection angles coincide very well with the experimental
 paths in the cases of zero and positive electric fields. Deviations of crack paths from simulation
 330 and experiment for negative fields are essentially attributed to the pronounced anisotropy of crack
 growth resistance in PZT-ceramics, which has so far been disregarded in the model. Compared to
 non-functional anisotropic structural materials, a modeling of fracture in ferroelectrics raises the
 difficulty that the axis of transverse isotropy is rotated locally as a result of domain switching and
 controlled by the solution of the nonlinear electromechanical boundary value problem.

335 Recordings with a high-speed camera provide insight into the process of crack initiation and

growth. A fundamental observation has thus been made, where the actual cracking is preceded by a white line, reminding of localization bands in ductile and quasi-brittle materials. The subsequent instable crack growth exhibits a substantially lower velocity than the one known from elastic surface waves in ceramic materials.

340 This research did not receive any specific grant from funding agencies in the public, commercial, not-for-profit sectors.

Appendix A. Material constants and Irwin matrix

The material constants for PZT-5H piezoelectric ceramics according to [32] are:

$$\begin{aligned}
 C_{1111} &= 126, & C_{1122} &= 55, & C_{2222} &= 126, \\
 C_{1133} &= 53, & C_{2233} &= 53, & C_{3333} &= 117, \\
 C_{1212} &= 35.5, & C_{1313} &= 35.3, & C_{2323} &= 35.3, \\
 e_{31} &= -6.5, & e_{15} &= 17, & e_{33} &= 23.3, \\
 \kappa_{11} &= 15.1, & \kappa_{33} &= 13.0,
 \end{aligned} \tag{A.1}$$

where the poling direction is parallel to the x_3 -axis and the units of the elastic moduli, the coupling coefficients and the dielectric permittivities are GPa, C/m² and C/(GVm), respectively.

The Irwin-matrix Y_{ij} solely depends on the material constants and the poling axis of the transversely isotropic piezoelectric ceramics. For the case of the experiment, where the poling direction is perpendicular to the initial crack, the Irwin-matrix and the characteristic matrix S_{ij} for the PZT-5H in-plane crack problem with the above units are defined as follows:

$$Y_{ij} = \begin{pmatrix} 1.755 \times 10^{-2} & 0 & 0 \\ 0 & 1.606 \times 10^{-2} & 1.277 \times 10^{-2} \\ 0 & 1.277 \times 10^{-2} & -4.578 \times 10^{-2} \end{pmatrix}, \tag{A.2}$$

$$S_{ij} = \begin{pmatrix} 0 & -1 & -0.287 \\ -1.124 & 0 & 0 \\ 0.022 & 0 & 0 \end{pmatrix}. \tag{A.3}$$

Table B.1: critical mechanical loading force (unit in N)

	$E = 0$	$E = 0.75E_c$	$E = -0.75E_c$
No.1	282.2	270.3	186.9
No.2	265.5	250.7	216.4
No.3	285.1	240.9	177.1
No.4	265.5	265.5	196.7
No.5	265.5	216.6	226.2
average	272.4	249	200.7

345 **Appendix B. Critical forces of crack initiation**

Table B.1 shows the critical mechanical loads of every test. For each loading condition, there were five specimens.

References

- [1] J. F. Scott, Applications of modern ferroelectrics, *Science* 315 (5814) (2007) 954–959.
- 350 [2] G. H. Haertling, Ferroelectric ceramics: History and technology, *Journal of the American Ceramic Society* 82 (4) (1999) 797–818.
- [3] R. F. Cook, S. W. Freiman, B. R. Lawn, R. C. Pohanka, Fracture of ferroelectric ceramics, *Ferroelectrics* 50 (1) (1983) 267–272.
- [4] S. W. Freiman, Mechanical behavior of ferroelectric ceramics, in: Sixth IEEE International
355 Symposium on Applications of Ferroelectrics, 1986, pp. 367–373.
- [5] K. Mehta, A. V. Virkar, Fracture mechanisms in ferroelectric-ferroelastic lead zirconate titanate (Zr: Ti=0.54:0.46) ceramics, *Journal of the American Ceramic Society* 73 (3) (1990) 567–574.
- [6] G. A. Schneider, V. Heyer, Influence of the electric field on Vickers indentation crack growth
360 in BaTiO₃, *J. Eur. Ceram. Soc.* 19 (6-7) (1999) 1299–1306.
- [7] F. Fang, W. Yang, Poling-enhanced fracture resistance of lead zirconate titanate ferroelectric ceramics, *Materials Letters* 46 (2-3) (2000) 131–135.

- [8] F. Fang, W. Yang, Indentation-induced cracking and 90° domain switching pattern in barium titanate ferroelectric single crystals under different poling, *Materials Letters* 57 (1) (2002) 198–202.
- [9] S. Hackemann, W. Pfeiffer, Domain switching in process zones of PZT, *Journal of the European Ceramic Society* 23 (1) (2003) 141–151.
- [10] A. G. Tobin, E. Pak, Effect of electric fields on fracture behavior of PZT ceramics, in: V. K. Varadan (Ed.), *Smart Structures and Materials 1993: Smart Materials*, SPIE Proceedings, SPIE, 1993, pp. 78–86.
- [11] S. B. Park, C. T. Sun, Fracture criteria for piezoelectric ceramics, *J. Am. Ceram. Soc.* 78 (6) (1995) 1475–1480.
- [12] D. Fang, Z.-K. Zhang, A. K. Soh, K. L. Lee, Fracture criteria of piezoelectric ceramics with defects, *Mechanics of Materials* 36 (10) (2004) 917–928.
- [13] H. Wang, R. N. Singh, Crack propagation in piezoelectric ceramics: Effects of applied electric fields, *J. Appl. Phys.* 81 (11) (1997) 7471–7479.
- [14] R. Fu, T. Y. Zhang, Effects of an electric field on the fracture toughness of poled lead zirconate titanate ceramics, *J. Am. Ceram. Soc.* 83 (5) (2000) 1215–1218.
- [15] C. T. Sun, S. B. Park, Measuring fracture toughness of piezoceramics by Vickers indentation under the influence of electric fields, *Ferroelectrics* 248 (2000) 79–95.
- [16] H. Cao, A. G. Evans, Electric-field-induced fatigue crack growth in piezoelectrics, *Journal of the American Ceramic Society* 77 (7) (1994) 1783–1786.
- [17] C. S. Lynch, L. Chen, Z. Suo, R. M. McMeeking, W. Yang, Crack growth in ferroelectric ceramics driven by cyclic polarization switching, *Journal of Intelligent Material Systems and Structures* 6 (2) (1995) 191–198.
- [18] I. Westram, A. Ricoeur, A. Emrich, J. Rödel, M. Kuna, Fatigue crack growth law for ferroelectrics under cyclic electrical and combined electromechanical loading, *J. Eur. Ceram. Soc.* 27 (6) (2007) 2485–2494.

- [19] G. Schneider, F. Felten, R. McMeeking, The electrical potential difference across cracks in PZT measured by Kelvin Probe Microscopy and the implications for fracture, *Acta Mater.* 51 (8) (2003) 2235–2241.
- [20] H. Jelitto, H. Keßler, G. A. Schneider, H. Balke, Fracture behavior of poled piezoelectric PZT under mechanical and electrical loads, *Journal of the European Ceramic Society* 25 (5) (2005) 749–757.
- [21] R. Fu, C.-F. Qian, T.-Y. Zhang, Electrical fracture toughness for conductive cracks driven by electric fields in piezoelectric materials, *Appl. Phys. Lett.* 76 (1) (2000) 126–128.
- [22] S. L. Santos e Lucato, D. C. Lupascu, J. Rödel, Effect of poling direction on R-curve behavior in lead zirconate titanate, *J. Am. Ceram. Soc.* 83 (2) (2000) 424–426.
- [23] A. Kolleck, G. A. Schneider, F. A. Meschke, R-curve behavior of BaTiO₃ and PZT ceramics under the influence of an electric field applied parallel to the crack front, *Acta Mater.* 48 (16) (2000) 4099–4113.
- [24] M. Kuna, A. Ricoeur, Theoretical investigation of fracture behaviour in ferroelectric ceramics, in: R. C. Bradt, D. Munz, M. Sakai, V. Y. Shevchenko, K. White (Eds.), *Fracture Mechanics of Ceramics*, Vol. 13, Springer US, Boston, 2002, pp. 63–82.
- [25] A. Ricoeur, M. Kuna, Influence of electric fields on the fracture of ferroelectric ceramics, *J. Europ. Ceram. Soc.* 23 (8) (2003) 1313–1328.
- [26] Y.-H. Seo, M. Vögler, D. Isaia, E. Aulbach, J. Rödel, K. G. Webber, Temperature-dependent R-curve behavior of Pb(Zr_{1-x}Ti_x)O₃, *Acta Materialia* 61 (17) (2013) 6418–6427.
- [27] W. S. Oates, C. S. Lynch, D. C. Lupascu, A. B. K. Njiwa, E. Aulbach, J. Rödel, Subcritical crack growth in lead zirconate titanate, *Journal of the American Ceramic Society* 87 (7) (2004) 1362–1364.
- [28] H.-S. Chen, H.-L. Wang, Y.-M. Pei, Y.-J. Wei, B. Liu, D.-N. Fang, Crack instability of ferroelectric solids under alternative electric loading, *Journal of the Mechanics and Physics of Solids* 81 (2015) 75–90.

- 415 [29] G. A. Schneider, Influence of electric field and mechanical stresses on the fracture of ferro-
electrics, *Annual Review of Materials Research* 37 (1) (2007) 491–538.
- [30] M. Acosta, N. Novak, V. Rojas, S. Patel, R. Vaish, J. Koruza, G. A. Rossetti, J. Rödel,
BaTiO₃-based piezoelectrics: Fundamentals, current status, and perspectives, *Applied Physics
Reviews* 4 (4) (2017) 041305.
- 420 [31] K. G. Webber, M. Vögler, N. H. Khansur, B. Kaeswurm, J. E. Daniels, F. H. Schader, Re-
view of the mechanical and fracture behavior of perovskite lead-free ferroelectrics for actuator
applications, *Smart Materials and Structures* 26 (6) (2017) 063001.
- [32] Y. E. Pak, Linear electro-elastic fracture mechanics of piezoelectric materials, *International
Journal of Fracture* 54 (1) (1992) 79–100.
- 425 [33] Z. Suo, C.-M. Kuo, D. Barnett, J. Willis, Fracture mechanics for piezoelectric ceramics, *Journal
of the Mechanics and Physics of Solids* 40 (4) (1992) 739–765.
- [34] H. Gao, T.-Y. Zhang, P. Tong, Local and global energy release rates for an electrically yielded
crack in a piezoelectric ceramic, *Journal of the Mechanics and Physics of Solids* 45 (4) (1997)
491–510.
- 430 [35] T. Y. Zhang, C. F. Gao, Fracture behaviors of piezoelectric materials, *Theoretical and Applied
Fracture Mechanics* 41 (1-3) (2004) 339–379.
- [36] L. Z. Jiang, C. T. Sun, Analysis of indentation cracking in piezoceramics, *Int. J. Solids Struct.*
38 (10-13) (2001) 1903–1918.
- 435 [37] L. Janski, M. Kuna, Adaptive finite element modeling of stationary and propagating cracks in
piezoelectric structures, *Arch. Mech.* 63 (5-6) (2011) 599–619.
- [38] J. Lei, L. Yun, T. Q. Bui, Numerical simulation of crack growth in piezoelectric structures by
BEM, *Engineering Analysis with Boundary Elements* 85 (2017) 30–42.
- 440 [39] C. Linder, C. Miehe, Effect of electric displacement saturation on the hysteretic behavior of
ferroelectric ceramics and the initiation and propagation of cracks in piezoelectric ceramics,
Journal of the Mechanics and Physics of Solids 60 (5) (2012) 882–903.

- [40] G. Sih, J. Zuo, Multiscale behavior of crack initiation and growth in piezoelectric ceramics, *Theoretical and Applied Fracture Mechanics* 34 (2) (2000) 123–141.
- [41] S. L. dos Santos e Lucato, H.-A. Bahr, V.-B. Pham, D. C. Lupascu, H. Balke, J. Rödel, U. Bahr, Electrically driven cracks in piezoelectric ceramics: experiments and fracture mechanics analysis, *Journal of the Mechanics and Physics of Solids* 50 (11) (2002) 2333–2353.
- [42] J. R. Rice, The localization of plastic deformation, in: W. Koiter (Ed.), *Theoretical and Applied Mechanics*, North-Holland Publishing Co., 1976, pp. 207–220.
- [43] D. A. DeAngelis, G. W. Schulze, Performance of PZT8 versus PZT4 piezoceramic materials in ultrasonic transducers, *Physics Procedia* 87 (2016) 85–92.
- [44] S. B. Park, C. T. Sun, Effect of electric field on fracture of piezoelectric ceramics, *International Journal of Fracture* 70 (3) (1993) 203–216.
- [45] H. Ma, Y. H. Chen, The explicit formulations for the J_k vector in both isotropic and anisotropic cases, *Int. J. Fracture* 75 (2) (1996) R25–R28.
- [46] L. Ma, A. M. Korsunsky, On the use of vector J -integral in crack growth criteria for brittle solids, *International Journal of Fracture* 133 (4) (2005) L39–L46.
- [47] P. O. Judt, A. Ricoeur, G. Linek, Crack path prediction in rolled aluminum plates with fracture toughness orthotropy and experimental validation, *Eng. Fract. Mech.* 138 (2015) 33–48.
- [48] P. O. Judt, J.-C. Zarges, M. Feldmann, A. Ricoeur, H.-P. Heim, Deflecting mode-I cracks in anisotropic materials, *Mechanics of Materials* 136 (2019) 103060.
- [49] F. Erdogan, G. C. Sih, On the crack extension in plates under plane loading and transverse shear, *J. Basic Eng.* 85 (4) (1963) 519–525.
- [50] M. E. Gurtin, *Configurational Forces as Basic Concepts of Continuum Physics*, Vol. 137, Springer New York, New York, 2000.
- [51] M. Kuna, *Finite Elements in Fracture Mechanics*, Vol. 201 of *Solid Mechanics and its Applications*, Springer Netherlands, Dordrecht, 2013.
- [52] Z. Wang, A. Ricoeur, Numerical crack path prediction under mixed-mode loading in 1D quasicrystals, *Theor. Appl. Fract. Mech.* 90 (2017) 122–132.